ACS OMEGA

Open Access

http://pubs.acs.org/journal/acsodf

Article

Deformation and Failure Characteristics of Strong−Weak Coupling Structures with Different Height Ratios Under Cyclic Loading and Unloading

Aikun Chen, Cheng Zhai,* Xu Yu, Yangfeng Zheng, Yuzhou Cong, and Jianguo Wu

Cite This: *ACS Omega* 2024, 9, 17076−17088

Read Online

ACCESS | Metrics & More | Article Recommendations

ABSTRACT: Strong−weak coupling outburst prevention technology can reduce the hazard of coal and gas outburst in mines based on hydraulic punching and grouting reinforcement. In this study, the mechanism of outburst hazards in the strong−weak coupling structure under mining disturbance was explored, and then cyclic loading and unloading experiments were performed on samples with different strong−weak height ratios (HRs) using the noncontact full-field strain testing (DIC) system and the acoustic emission (AE) system. The results show that the failure strength of the sample gradually increases with the increase in HR. The residual strain of the strong and weak structures undergoes three stages, i.e., the decelerated deformation, the constant-velocity deformation, and the accelerated deformation. Deformation mainly occurs in the weak structure and starts at the strong−weak interface. The AE signals present strong regional distribution characteristics and the Felicity effect, and the damage is concentrated near 70% of each stage in the cyclic loading process. As the HR rises, the weak structure transitions from brittle damage to ductile damage and from shear damage to tensile damage. In addition, due to the difference in Poisson effects of strong and weak structures, the strong structure transitions from a unidirectional stress state to a triaxial tensile−compressive stress state. When the HR increases to 85:15, the strong structure undergoes tensile damage.

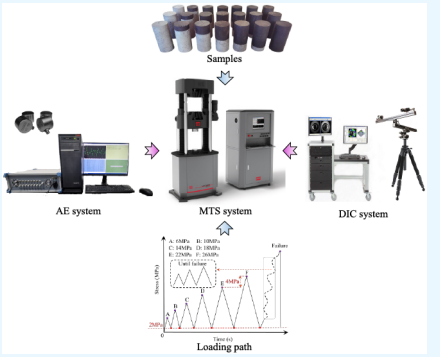

1. INTRODUCTION

Coal accounts for about 95% of China's total fossil energy resources. In 2021, the annual coal production was 4.13 billion tons, demonstrating its primary role in China's energy mix.[1−3] However, over 30% of coal mines in China have a high gas content, which can easily trigger gas accidents. Coal and gas outburst (hereafter termed outburst) means that massive gas and broken coal gush into a limited working space within a short time during mining. It is a complex dynamic disaster that can easily cause considerable casualties and economic loss.[4−6] Statistics reveal that over half of the world's outburst accidents occurred in China, making China the country with the highest outburst hazard. At present, as shallow coal reserves are increasingly depleted in China, coal mining is shifting toward the deep area at a speed of 20−30 m per year. Deep coal mining is accompanied by 'three highs and one disturbance' (high ground stress, high ground temperature, high osmotic pressure, and strong mining disturbance), which aggravates outburst hazards.[6−8] The year 2021 witnessed 6 outburst accidents with 24 deaths in China. The frequent occurrence of accidents demonstrates the limitations of the current theory and technologies in preventing outbursts in coal mining.[9,10]

Gas pre-extraction technology can effectively prevent outbursts.[11−14] However, 70% of coal seams in China, especially those in deep formations, are of low permeability, high adsorption capacity, and high in situ stress. Conventional gas extraction technologies fail to perform well under such conditions. Therefore, it is necessary to take artificial permeability enhancement measures for coal seams. Hydraulic punching is widely adopted in mine gas control,[15−18] as it flushes out the broken coal in the coal seam by jetting high-pressure water, forming a large volume of cavity, releasing the in situ stress, and effectively enhancing coal permeability. However, the punching-induced reduction in the strength of the coal body around the borehole may hinder bolt support during roadway excavation. Grouting reinforcement can improve the bearing capacity of the roadway surrounding rock by injecting cement slurry into the coal seam, which effectively improves the supporting effect of the bolt.[19] The injected cement slurry can improve the mechanical strength of the coal seam and meanwhile lower the permeability and compressibility. It can not only improve the support effect on the roadway surrounding rock but also block methane

Received: November 5, 2023
Revised: February 19, 2024
Accepted: February 22, 2024
Published: April 2, 2024

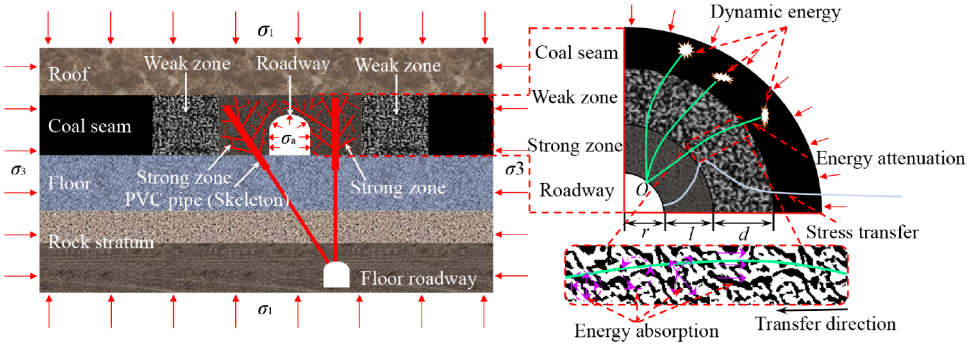

Figure 1. Mechanical control model for strong−weak coupling outburst under mining disturbance.

channels, hence reducing or eliminating outbursts.[20−22] Therefore, after hydraulic punching and gas drainage, cross-measure boreholes are constructed from the floor roadway to the two sides of the coal roadway, and then polyvinyl chloride (PVC) pipes are inserted into the boreholes as a strong and tough skeleton. Subsequently, the coal and two sides of the roadway are strengthened by grouting to form a strengthening zone. In this way, a strong−weak coupling structure composed of a relatively near grouting strengthening zone and a relatively far hydraulic punching weakening zone is formed on both sides of the roadway to prevent roadway instability accidents.

Nowadays, researchers mainly study the deformation and failure characteristics of strong−weak coupling structures with the coal−rock combination. The results show that the deformation and failure characteristics of a coal−rock combination during uniaxial compression are mainly controlled by coal. The uniaxial compressive strength (UCS) and elastic modulus of the coal−rock combination are slightly larger than those of coal. Most of the cracks in coal arise from uniaxial compression,[23] and cracks generated by the failure of coal trigger the failure of rock.[24] The dynamic stress−strain curves of coal−rock combination in the high loading rate range present bimodal characteristics: the first peak stress is independent of the loading rate, while the dynamic compressive strength (second peak stress) and dynamic peak strain (second peak strain) increase linearly with the loading rate.[25] Based on effective medium theory, a binary effective medium model for the composite under triaxial compression experimental conditions was established by the researchers. The model's reliability was subsequently validated through compression experiments conducted on a concrete−granite composite.[26] In addition, by conducting uniaxial compression experiments with cement and gypsum-poured samples as strong and weak structures, respectively, researchers found that the strong−weak coupling structure could effectively transfer the peak stress from the coal roadway to a farther area and enhance the ability to resist roadway deformation.[21]

Problems remain despite massive experimental and theoretical works on strong−weak coupling structures. For example, the deformation and failure characteristics of strong−weak coupling structures with different height ratios (HRs) under the disturbance of periodic mining stress is still unclear. The coal roadway is subject to periodic stress disturbance during working face mining, resulting in deformation, damage, and even failure,[27,28] and the instability and damage of the roadway are the prerequisites for the occurrence of outbursts in mining.[29] The layout parameters of the strong and weak zones may directly affect the overall failure process of the strong−weak coupling structures and thus influence the outburst prevention effect.

In this study, the mechanism of the outburst hazard of strong−weak coupling structures under mining disturbances was investigated. Then, cyclic loading and unloading experiments were conducted on the strong−weak coupling samples with different HRs by a hydraulic rock mechanic testing machine (MTS). Furthermore, the full-field deformation and failure characteristics of the samples were monitored by the noncontact full-field strain testing (DIC) system and the acoustic emission (AE) monitoring system. The research results boast great significance for designing strong−weak coupling structures in field engineering practice, improving the stability of roadways during working face mining, and preventing outburst dynamic disasters.

2. OUTBURST PREVENTION THEORY OF STRONG−WEAK COUPLING STRUCTURE UNDER MINING DISTURBANCE

Before the outburst, the roadway surrounding rock is close to the ultimate bearing state under the action of both static load stress field and gas energy. After a new dynamic load stress field is generated by mining activities, the superimposed stress field of dynamic-static load and residual gas internal energy after pre-extraction exceeds the ultimate bearing strength of roadway surrounding rock under the action of the above three. Resultantly, the roadway surrounding rock is destroyed suddenly, throwing coal and gas. The outburst prevention method of the strong−weak coupling structure under mining disturbance is shown in Figure 1.

The minimum energy consumed for failure in the strong zone is

$$E_{\min} = \frac{\sigma_c^2}{2E} \tag{1}$$

The elastic energy of the strong zone under the 3D stress state (under static load) is

$$E_0 = \frac{\sigma_1^2 + \sigma_2^2 + \sigma_3^2 - 2\nu(\sigma_1\sigma_2 + \sigma_1\sigma_3 + \sigma_2\sigma_3)}{2E} \tag{2}$$

After the generation of dynamic load, the elastic energy accumulated in the strong zone is[30]

$$E_J = E_0 + \sum \Delta E_{Di} \tag{3}$$

where σ_c and E are the uniaxial compressive strength and the elastic modulus, respectively; σ_1, σ_2, and σ_3 are the three

https://doi.org/10.1021/acsomega.3c08786
ACS Omega 2024, 9, 17076−17088

principal stresses; ν is the Poisson's ratio; ΔE_{Di} is the change in elastic energy accumulated under the ith dynamic load.

According to Figure 1, as mining proceeds, the coal seam generates periodic dynamic load energy and transfers it to the center of the roadway. The energy is greatly absorbed when it is transferred to the weak zone. It is assumed that the dynamic load energy generated under the ith dynamic load is E_{di}, and the energy transmitted to the roadway side under the ith dynamic load is

$$E_{Di} = E_{di}(h_i - d - l - r)^{\eta_1} d^{\eta_2} l^{\eta_3} \quad (4)$$

where d and l are the lengths of the weak zone and the strong zone, respectively; r and h_i are the distances from the central point of the roadway to the roadway side and the dynamic load point under the ith load, respectively; η_1, η_2, and η_3 are energy attenuation indexes in the coal seam, the weak zone, and the strong zone, respectively.

Thus, the total energy transmitted to the roadway side is

$$E_D = \sum E_{Di} \quad (5)$$

After hydraulic punching and gas drainage, the pressure is released, and the gas energy declines.[31,32] The residual gas energy acting on the roadway is

$$E_g = E_{g0} - \Delta E_g \quad (6)$$

where E_{g0} and ΔE_g are the original gas energy and the variation after hydraulic punching and gas drainage, respectively.

Therefore, the total energy acting on the roadway side during mining is

$$E_a = E_J + E_D + E_g \quad (7)$$

Ulteriorly, the energy criterion for roadway outburst during mining is

$$E_a = E_J + E_D + E_g \geq E_{min} \quad (8)$$

The strong−weak coupling outburst prevention technology reduces the elastic energy by relieving stress and transferring it to the stress concentration area and reduces the transmitted dynamic load energy through energy absorption by the weak zone. Hydraulic punching and gas drainage weaken the internal energy of gas, while grouting reinforcement raises the minimum energy of failure in the strong zone. Hence, the technology can effectively alleviate roadway deformation and prevent outbursts.

3. MATERIALS AND METHODS

3.1. Sample Preparation. The strong structure was made of high-strength Portland cement (62.5, cylindrical samples of ϕ50 mm × 100 mm, water−cement ratio 0.4) and was kept in a constant-temperature-and-humidity curing box for 28 days. The weak structure was raw coal (cylindrical samples of ϕ50 × 100 mm, taken perpendicular to the bedding direction with a core drilling machine). Finally, samples were cut according to the designed strong−weak HRs and then bonded with epoxy resin AB glue to form a strong−weak coupling structure (Figure 2). The samples were divided into 7 groups (3 samples in each group), namely, a briquette coal group, a raw coal group, and 5 strong−weak coupling groups with different HRs. The briquette coal group and the raw coal group are designed for the basic mechanical determination of strong and weak structures, yet the 5 strong−weak coupling groups are for the cyclic loading and unloading tests. The strong−weak coupling groups were set according to HRs of 15:85, 30:70, 50:50, 70:30, and 85:15 and labeled as $S_{15}W_{85}$, $S_{30}W_{70}$, $S_{50}W_{50}$, $S_{70}W_{30}$, and $S_{85}W_{15}$, respectively. The basic mechanical parameters of the briquette coal group and the raw coal group are given in Table 1.

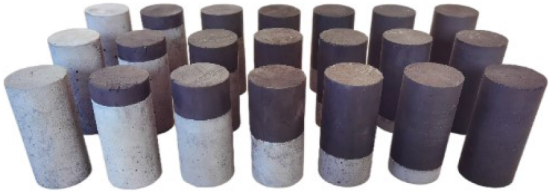

Figure 2. Experimental samples.

Table 1. Mechanical Parameters of the Briquette Coal Group and the Raw Coal Group

sample type	compressive strength/MPa	elastic modulus/GPa	Poisson's ratio	density/ g·cm^{-3}
briquette coal	64.58	7.03	0.19	2.36
raw coal	7.88	1.34	0.34	1.63

3.2. Experimental System. The experimental system (Figure 3) comprises three subsystems: a MTS system (C64.605, MTS Systems Co., Ltd.), a DIC system (VIC-3D, American CSI Technology Co., Ltd.), and an AE system (DS5-16C, Beijing Soft Island Technology Co., Ltd.). The MTS system has two parts: loading and control. In this experiment, the force control method is adopted for loading, and the inlet force and the loading rate are set to 0.05 and 1.5 kN/s, respectively. The DIC system consists of an LED light source, a high-speed camera, and a data analysis system (for simultaneous acquisition of DIC and MTS data), and the sampling frequency is set to 2 Hz. The AE system is composed of RS-2A sensor probes, a preamplifier, and a data acquisition and analysis system. The input signal range is ±10 V, and the sampling rate is 10 MHz. Considering noise, the threshold is set to 30 dB. The experimental system can achieve real-time synchronous acquisition of full-field strain and AE characteristics during sample loading.

3.3. Experimental Process and Loading Path. *3.3.1. Experimental Process.* (1) Speckles were sprayed on the samples with the speckle processing tool of the VIC-3D system.

(2) The sprayed samples were successively placed on the MTS testing platform. To eliminate the end-face effect, the Vaseline coupling was applied to both ends of the samples.

(3) Two AE probes were stuck to the strong structure and the weak structure. Considering the cylindrical shape, the Vaseline couplant was also used on the contact area between the AE probes and the samples to avoid weak signaling.

(4) Multistage cycling loading and unloading was applied with the MTS controller, during which the data were synchronously acquired by the AE monitoring system and the VIC-3D system until the sample failed.

(5) Finally, the full-field data were analyzed in VIC-3D 9.0 software. The AE data were exported to determine sample failure.

3.3.2. Loading Path. The periodic mining stress disturbance of coal was simulated by multistage cyclic loading and unloading. In the simulation, the loading rate was 0.5 kN/s; the stress difference between adjacent cycles was 4 MPa; and

https://doi.org/10.1021/acsomega.3c08786
ACS Omega 2024, 9, 17076−17088

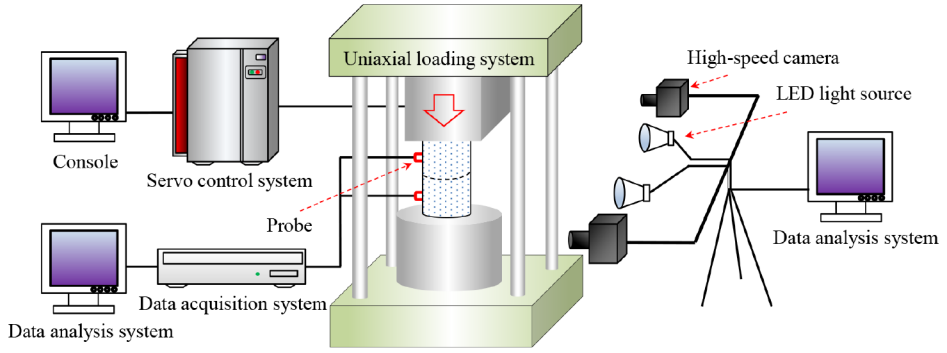

Figure 3. Experimental system.

the stress peak points of each cycle were recorded as A, B, C, D, etc. When the load reached the corresponding stress peak, the stress was unloaded at a rate of 0.5 KN/s to 2 MPa for the next cycle of loading until the sample was damaged. The loading path is shown in Figure 4.

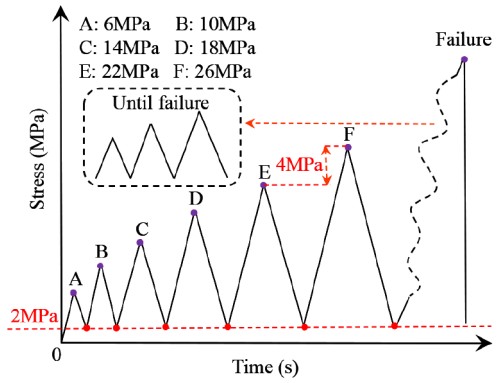

Figure 4. Sample loading path.

4. RESULT ANALYSIS AND DISCUSSION

4.1. Failure Strength. Figure 5 shows the failure strength of the strong−weak coupling samples with different HRs under cyclic loading and unloading. The failure strength increases gradually with the increase of HR. The failure strength of group $S_{85}W_{15}$ (44.37 MPa) is 391.91% higher than that of group $S_{15}W_{85}$ (9.02 MPa). The strength of the strong−weak coupling samples gradually transfers from the weak structure to the strong structure. Thus, raising the grouting range can effectively improve the roadway stability in the strong−weak coupling section under mining disturbance and enhance the ability of the roadway to resist the hazard of outburst during mining.

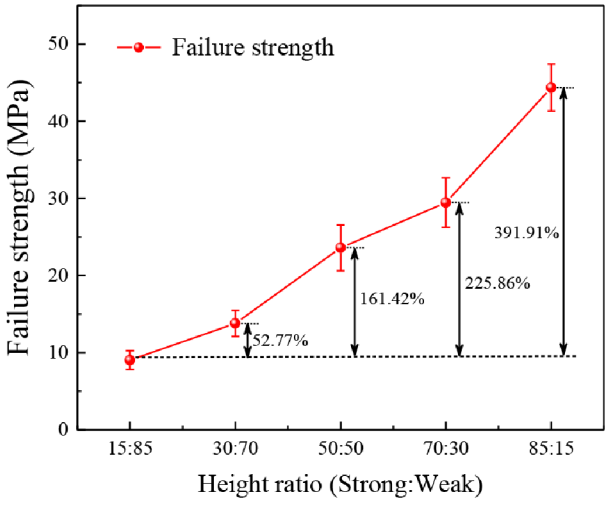

Figure 5. Failure strength of strong−weak coupling samples.

4.2. Full-Field Deformation of Strong−Weak Coupling Samples. *4.2.1. Lateral Strain.* The DIC technology involves capturing two digital images of a sample before and after deformation and computing of the changes in digital image points within the relevant regions of interest to obtain comprehensive deformation information on the sample. This method offers nondestructive and high-precision advantages.[33,34,46] By monitoring the sample's surface during the loading and unloading processes, the full-field strain characteristics of the sample have been obtained[35] (Figures 6 and 7). The strain field programs in the loading process and at the moment of failure were extracted at the peak stress point of each loading stage by a VIC-3D high-speed camera.

After the strains were calibrated and calculated using Vic-3D 9 software on the images collected during the loading and unloading processes of the samples, lateral and axial strain cloud maps of the samples were obtained. Figure 6 displays the distribution of the lateral strain field of the strongly weakly coupled samples under cyclic loading and unloading. In the loading process, large strain occurs in the weak structure, while small strain occurs in the strong structure. As the HR rises, the strain zone shows a delay effect. Groups $S_{15}W_{85}$, $S_{30}W_{70}$, $S_{50}W_{50}$, and $S_{70}W_{30}$ exhibit strain concentration areas at point A, while group $S_{85}W_{15}$ presents such a phenomenon at point C, which suggests that an increase in HR strengthens the resistance of the weak structure to deformation. In addition, the shape of the weak structure strain zone is irregular during loading, and this phenomenon gradually intensifies as the proportion of the weak structure grows, which mainly results from the anisotropy of the coal. The increase in the proportion of the weak structure is equivalent to the increase in the deformable domain of the sample and the randomness of failure; the sample can experience more forms of deformation and failure in a wider range (referring to Section 4.3.34.3.3). It is noted that for group $S_{85}W_{15}$ at point J, the strong structure has a strain concentration area near the strong−weak interface and is finally destructed. This indicates that when the disturbance effect is strong enough to damage the strong structure during mining, damage starts from the vicinity of the strong−weak interface.

https://doi.org/10.1021/acsomega.3c08786
ACS Omega 2024, 9, 17076−17088

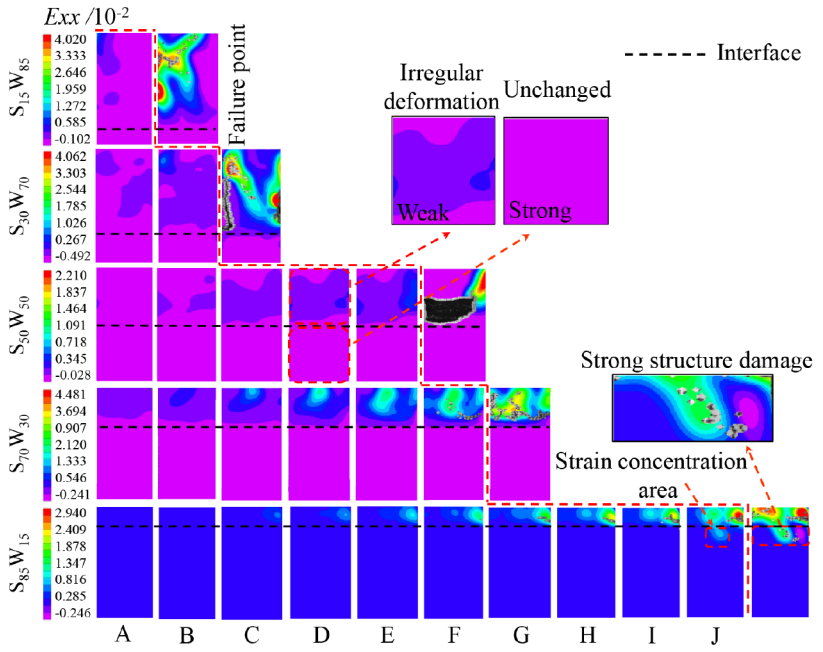

Figure 6. Distribution of the lattice-tension Gaussian strain in strong−weak coupling samples.

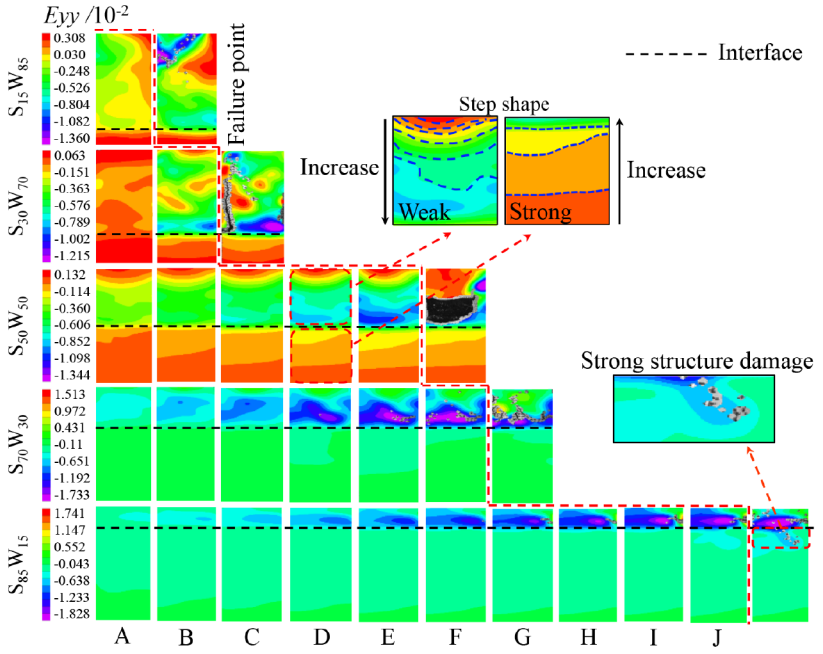

Figure 7. Distribution of axial strain in strong−weak coupling samples.

4.2.2. Axial Strain. Figure 7 shows the distribution of the axial strain field of the samples. Similar to the lateral strain, the axial strain of the strong−weak coupling samples is mainly concentrated in the lower half of the weak structure, that is, near the strong−weak interface. From the strain field nephograms at the peak stress points and at the moment of failure, it is found that the strain concentration area before the peak stress point of groups $S_{15}W_{85}$ and $S_{30}W_{70}$ cannot predict the failure crack area, which is attributed to the brittleness[36] and nonhomogeneity of coal; in contrast, the failure of groups $S_{50}W_{50}$, $S_{70}W_{30}$ and $S_{85}W_{15}$ develops along the strain concentration area, which can be explained from two aspects. First, as the proportion of the weak structure decreases, both the deformable domain of the sample and the randomness of deformation decline to a certain extent so that the weak structure can withstand higher stress. In this case, under the action of high stress, the samples fail progressively along the strain concentration area. Second, a rising HR changes the failure mode of the weak structure from brittle failure to ductile failure, resulting in severer deformation of the weak structure at the moment of failure. It can also be seen that the strain value in the vicinity of the two ends is generally smaller than that near the strong−weak interface, especially for group $S_{50}W_{50}$, which forms a step shape. Consequently, damage occurs near the interface, causing an energy release. This demonstrates that under the action of mining stress, the failure of the weak

https://doi.org/10.1021/acsomega.3c08786
ACS Omega 2024, 9, 17076−17088

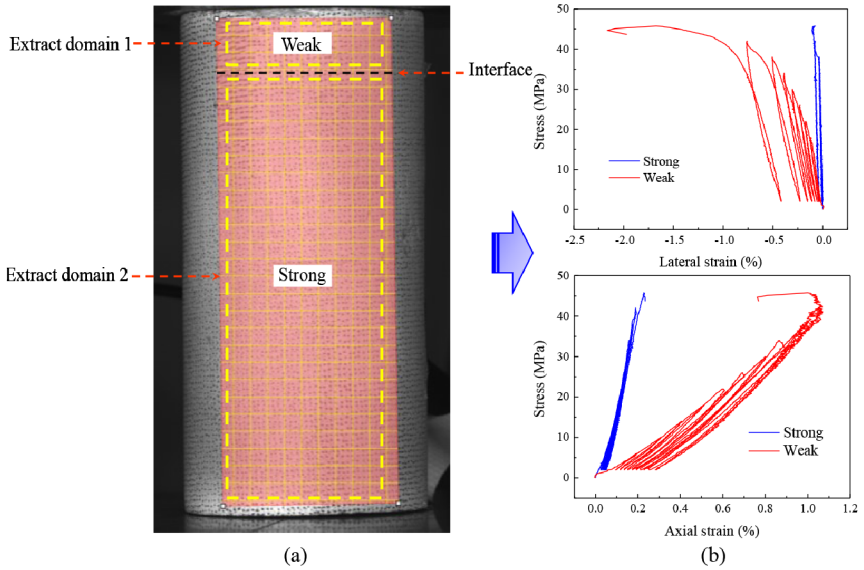

Figure 8. Strain extraction method and results of typical strong−weak coupling samples ($S_{85}W_{15}$), where (a) and (b) denote the strain extraction method and strain extraction results, respectively.

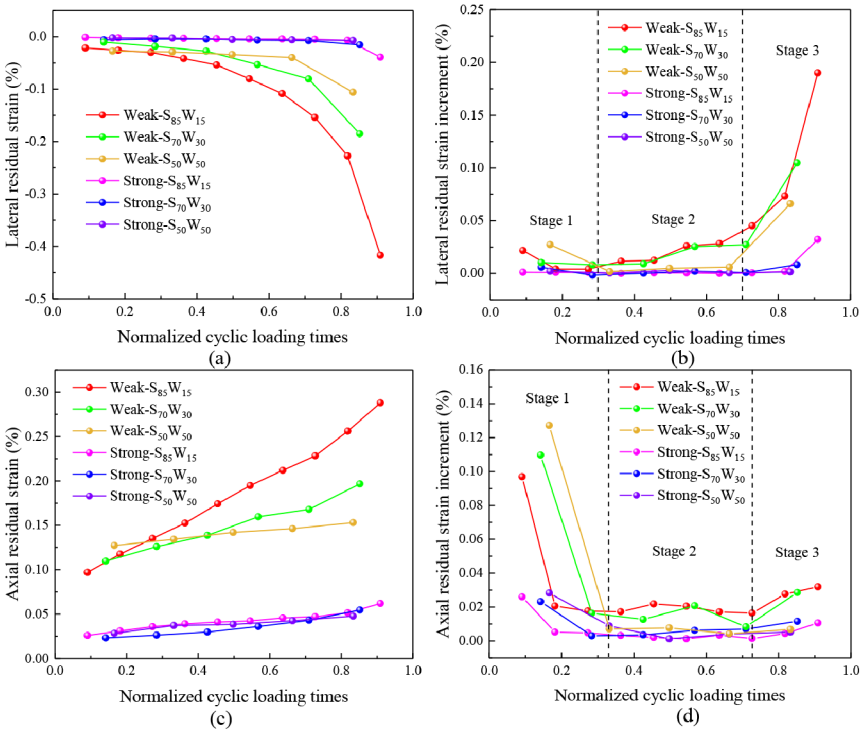

Figure 9. Residual strain and increment curves of strong−weak coupling samples, where (a) and (b) denote the lateral residual strain and its increment, respectively, and (c) and (d) denote the axial residual strain and its increment, respectively.

structure starts from the strong−weak interface and gradually proceeds toward the direction away from the roadway. Such a failure sequence prevents part of the energy from being transferred to the roadway. The remaining energy is transferred to the strong structure with a relatively high strength. The strong structure resists residual stress and effectively safeguards the overall stability of the roadway during mining.

4.2.3. Residual Strain. The strain extraction method during cyclic loading and unloading using the VIC-3D software (with $S_{85}W_{15}$ as an example) is illustrated in Figure 8a, based on which the strains of the weak structure (extraction domain 1) and the strong structure (extraction domain 2) were analyzed, respectively. The stress−strain curves of typical samples ($S_{85}W_{15}$) are displayed in Figure 8b. As can be seen from Figure 8b, the curves gradually shift toward the direction of increasing strain, and the strong and weak structures form hysteresis loops, suggesting that each level of loading can cause damage. The deformation and hysteresis loops of the weak structure are significantly larger than those of the strong structure, indicating that the weak structure accumulates more intense damage by cyclic loading and unloading and undergoes obvious fatigue damage inside. As loading continues, the

https://doi.org/10.1021/acsomega.3c08786
ACS Omega 2024, 9, 17076−17088

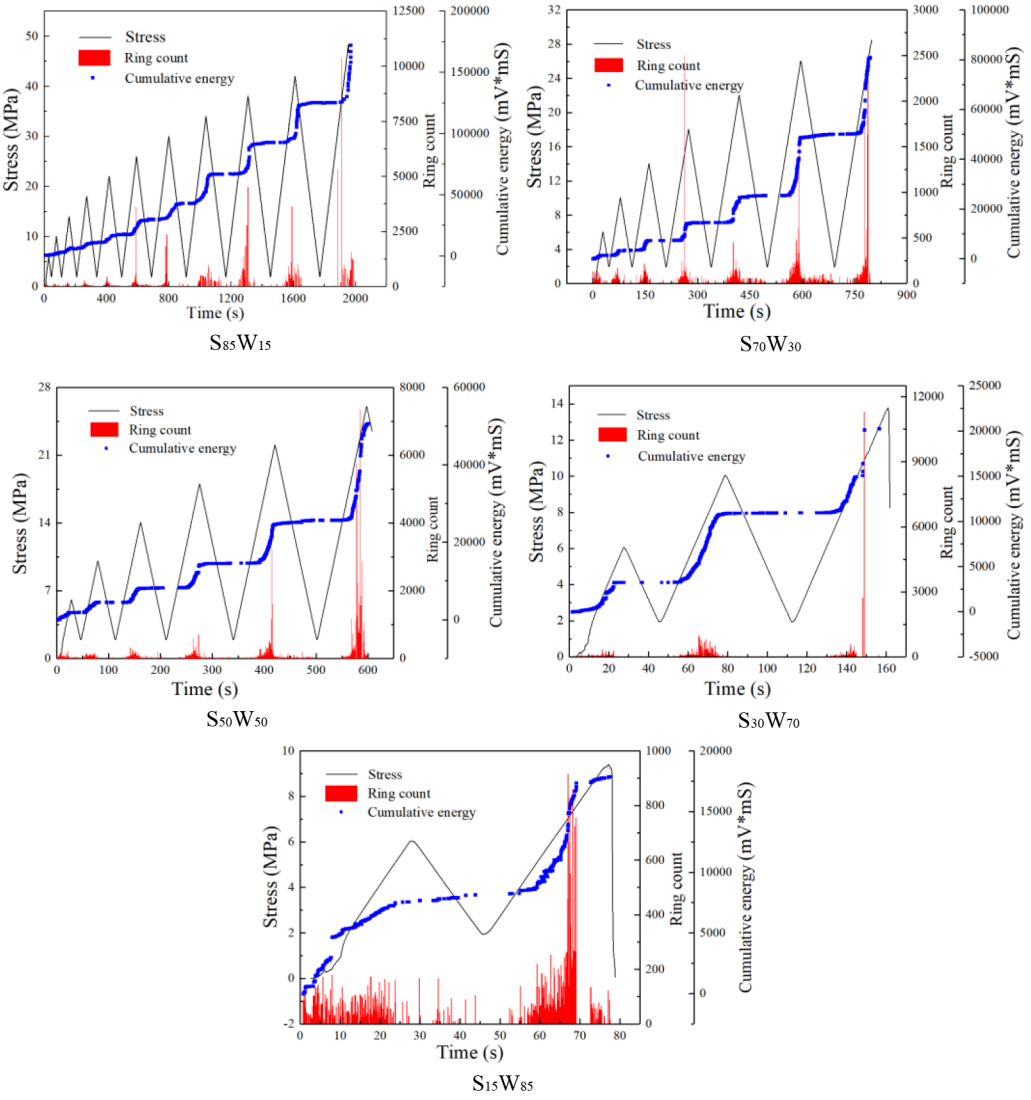

Figure 10. AE ring count and accumulated energy curves of strong−weak coupling samples.

cohesion between the fractured surfaces is gradually lost, and the bearing capacity is mainly provided by the friction between the fractured surfaces. Due to the large number of fractured surfaces, the frictional force and external force between the fractured surfaces are constantly adjusted for stress. When a new equilibrium is reached, the weak structure still holds a certain bearing capacity, and the residual strain level is further improved. However, the strong structure produces mild deformation in each loading stage and returns to the initial level in the unloading stage, generating a small residual strain. Therefore, under cyclic loading and unloading, the weak structure deforms and is damaged to absorb energy, while the strong structure resists both deformation and residual energy, effectively protecting the roadway surrounding rock.

Figure 9 shows the residual strain and increment curves of groups $S_{50}W_{50}$, $S_{70}W_{30}$ and $S_{85}W_{15}$ after normalized cycle times, where the normalized cycle times refer to the ratio of the actual cycle times to the total cycle times. The residual strain value of the strong structure is notably smaller than that of the weak structure, and the weak structure generates residual strain in each cyclic loading stage, which is similar to the typical curve of the three-stage deformation of rock mass.[37] The strong and weak structures share similar variation trends; that is, both of them are nonlinearly correlated with the number of cycles. The curves can be roughly divided into three stages based on the incremental variation of the residual strain of the weak structure: the decelerated deformation stage (0−0.3 times), the constant-velocity deformation stage (0.3−0.7 times), and the accelerated deformation stage (0.7−1.0 times).

(1) According to Figure 9, the weak structure mainly suffers from axial deformation in the decelerated deformation stage with slight lateral deformation. As illustrated in Figure 9b,d, the residual deformation increment gradually decreases in such a stage. The axial residual increment of group $S_{50}W_{50}$ decreases from 0.129% to 0.062%, as a result of gradual compaction of microcracks inside the sample during cyclic loading of a lower stress. In the first loading, cracks are compacted the most quickly. As the number of cycles grows, the internal structure gradually becomes denser; the compaction slows down; and the residual deformation increment gradually decreases. The strong structure experiences similar lateral deformation to the weak structure yet with a much smaller value. In this stage, the strong structure produces only small compaction in the axial direction. For example, the axial residual strain of group $S_{85}W_{15}$ increases from 0.027% to 0.035%, and the axial residual strain increment decreases from 0.026% to 0.004%. The stress in this

https://doi.org/10.1021/acsomega.3c08786
ACS Omega 2024, 9, 17076−17088

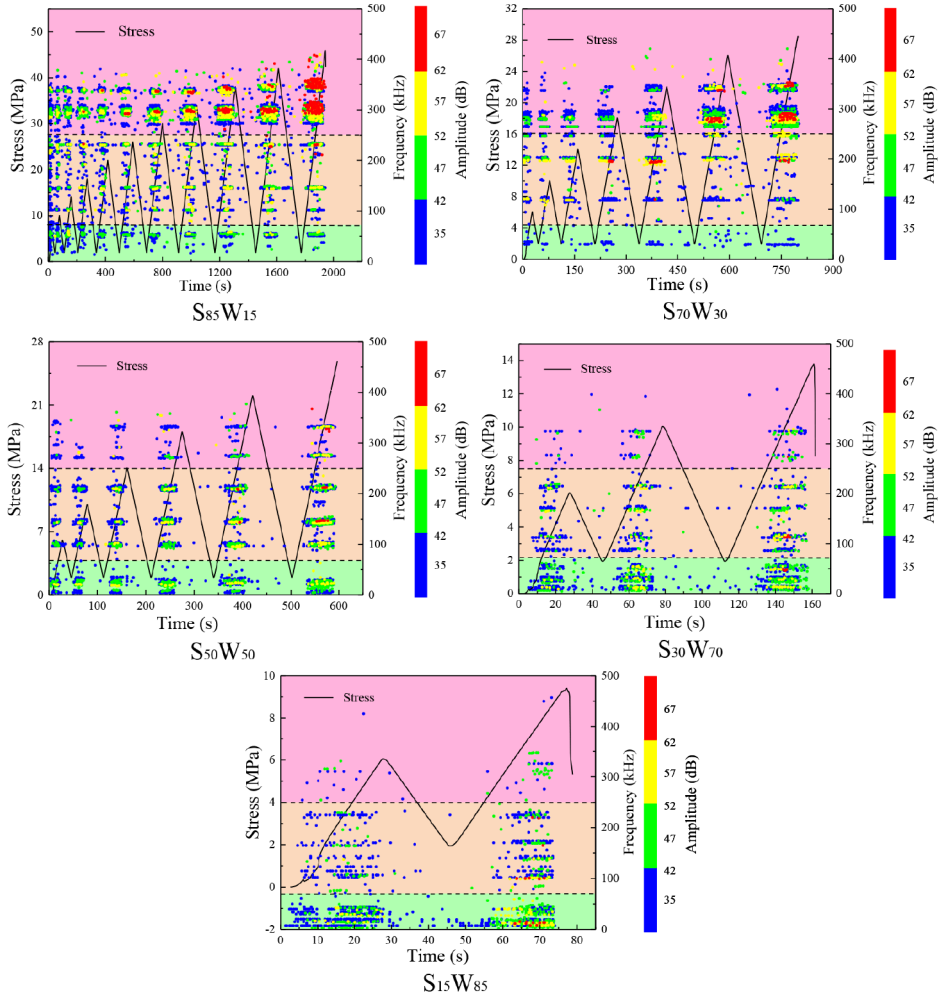

Figure 11. Dominant frequency−amplitude distribution of AE waveforms of samples.

stage cannot lead to lateral expansion, so the lateral residual strain hardly changes.

(2) In the constant-velocity deformation stage, the strong and weak structures with axial residual strain both rise steadily at a constant velocity. As the number of cycles and the stress rise, microcracks in the weak structure begin to expand, and they connect in a small range, leading to a slight increase in lateral residual strain. For the strong structure, the stress remains in the stage of primary crack compaction; consequently, the lateral residual strain hardly changes, and the axial residual strain increases by less than 0.01%.

(3) In the accelerated deformation stage, the axial and lateral residual strains of the strong and weak structures both show an accelerated increase, yet those of the weak structure increase more remarkably. The maximum value of the lateral residual strain increment of the group $S_{85}W_{15}$ is up to 0.186%, because after the residual strain reaches a certain value, microcracks inside the weak structure gradually connect, resulting in a surge of residual strain before failure. It is noticed that the lateral strain of the strong structure of group $S_{85}W_{15}$ jumps before failure, from 0.004% to 0.032%, which is attributable to the difference in the Poisson effects of the strong and weak structures. The weak structure expands first, applying a friction force to the strong structure at the interface, which is directed toward the center of the interface, equivalent to the tensile stress of the strong structure outward from the central axis. When the friction force reaches a certain value, tensile cracks occur inside the strong structure, resulting in a jump in the lateral residual strain of the strong structure before failure.

In addition, in the whole loading process, the lateral and axial residual strains of the weak structure gradually increase with the rise of HR, that is, $S_{85}W_{15} > S_{50}W_{50} > S_{70}W_{30}$. The lateral and axial residual strains of group $S_{70}W_{30}$ before failure are 0.116% and 0.158% respectively, while those of group $S_{85}W_{15}$ are relatively higher, 0.426% and 0.287%, respectively, which suggests that an increase in HR transforms the weak structure from brittle damage to ductile damage.

4.3. AE Characteristics. *4.3.1. AE Time Domain.* When alterations occur within the internal structure of a material, stress undergoes a sudden redistribution, leading to the generation of transient elastic waves. AE technology, as a nondestructive testing technique, aims to characterize the fracture mechanism of coal−rock masses by detecting the elastic waves released during the deformation and propagation of cracks within the material under stress.[38,39] Monitoring the characteristic parameters of internal damage within samples during the loading and unloading processes allow for the derivation of ring counts and cumulative energy features of the samples (Figure 10), thereby providing insights into the material's behavior. The ring count refers to the number of times the AE signal exceeds a predetermined threshold, serving as an acoustic reflection of the evolution of the internal

https://doi.org/10.1021/acsomega.3c08786
ACS Omega 2024, 9, 17076−17088

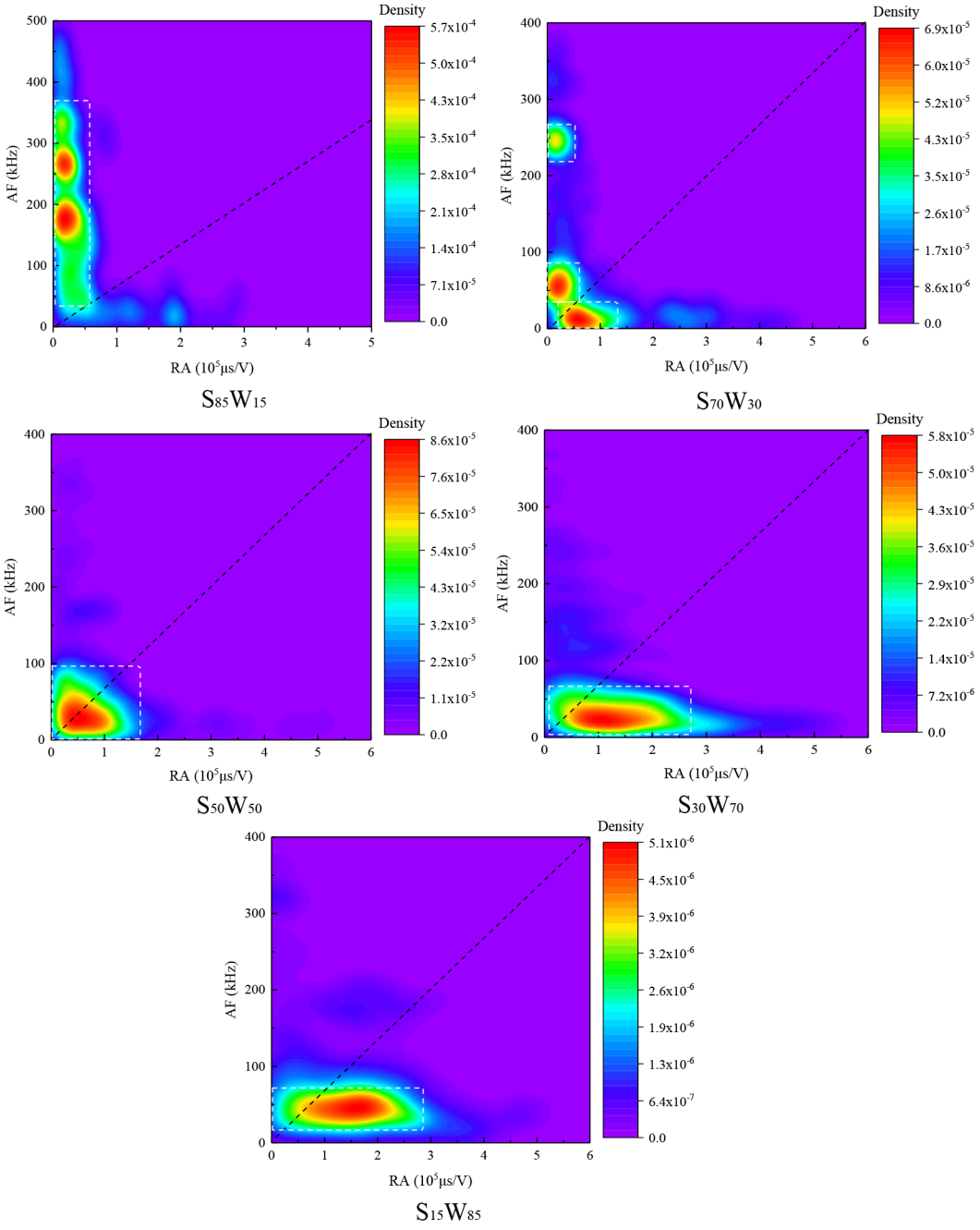

Figure 12. AF−RA data density maps of samples with different HRs.

structure within the sample, while the energy indicates the energy released by crack expansion inside the sample per unit time.[40,41]

As exhibited in Figure 10, the AE signals of samples show strong regional distribution characteristics under cyclic loading and unloading. The AE ring counts are concentrated near 70% in each stage in the cyclic loading process. Before reaching the stress peak, the AE ring count decreases and is not active in the unloading stage of each cycle, where the AE signals step into a quiet period. When the AE signals appear in the next cycle, the stress value becomes significantly lower than the maximum stress value loaded in the previous stage, so that the AE signals exhibit the Felicity effect.[42] For example, the AE signal of group $S_{50}W_{50}$ appears at 17.43 MPa in the last stage of loading, which is significantly lower than the maximum loading stress (22 MPa) in the previous stage. This phenomenon can be explained as follows: under the action of axial stress, the weak structure is in a yielding or unstable state; in this case, pores and cracks emerge continuously, and local damage and slippage of the rupture surface generate AE signals. The AE signals are abnormally active near 70% of each stage in the cyclic loading process. Meanwhile, the sample with a larger proportion of the weak structure corresponds to a greater number of cycles. The AE ring count changes abruptly near the 70% point. For example, group $S_{85}W_{15}$ experiences abrupt changes at 588 s (sixth cycle), 793 s (seventh cycle), 1,321 s (eighth cycle), and 1,610 s (ninth cycle), which is small-scale damage of the weak structure. As the HR grows, the failure of the weak structure requires a greater stress, and thus the sample can withstand more cycles of loading and unloading

https://doi.org/10.1021/acsomega.3c08786
ACS Omega 2024, 9, 17076−17088

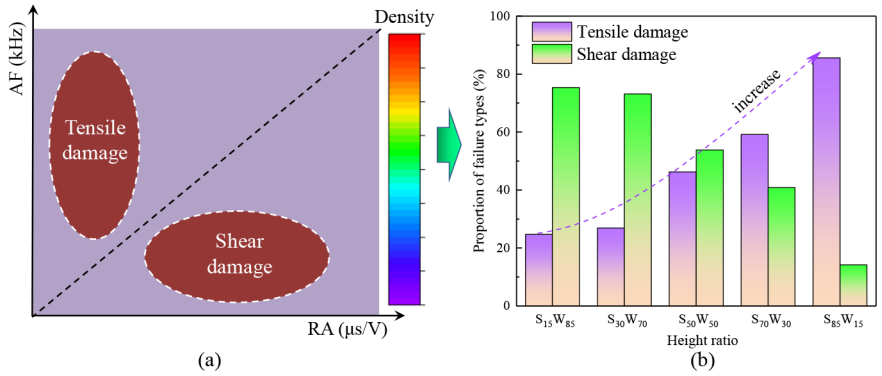

Figure 13. (a) Classification of damage types. (b) Percentages of damage modes of samples with different HRs.

and gradually transitions from brittle damage to ductile damage. Therefore, when the peak stress of loading at each level is reached, the weak structure is damaged macroscopically on a small scale. The damage means the release of energy, which is reflected by a sharp rise in the energy curve. After multistage cyclic loading and unloading, the energy is gradually released. As a result, less energy is transferred to the strong structure, which effectively alleviates the outburst hazard.

4.3.2. AE Frequency Domain. The dominant frequency and corresponding amplitude of AE waveforms can reflect the fracture information in the process of rock failure and fracturing, which provides a new perspective for exploring the fracture behaviors of samples with different HRs.[38,41] Accordingly, the dominant frequency and amplitude of the AE waveforms can be calculated by the Fast Fourier transform (FFT) algorithm. Figure 11 gives the dominant frequency−amplitude distribution of the samples. Both the dominant frequency and amplitude of AE waveforms gradually rise with the increase in HR. For example, for groups $S_{15}W_{85}$ and $S_{30}W_{70}$, the dominant frequency of AE waveforms is mainly distributed in the low-frequency region (0−75 kHz), and the middle-frequency region (0−250 kHz), and few signal clusters appear in the high-frequency region (300−500 kHz). With reference to Figures 6 and 7, low-amplitude AE signals mostly appear in the initial loading stage, which are mainly generated by gradual closure of cracks in the weak structure. As the number of cycles grows, the AE signals shift to a higher amplitude, which means that after the stress threshold of crack initiation in each area inside the weak structure is reached, high-amplitude AE signals are gradually emitted. Particularly, a few AE waveforms higher than 62 dB occur before failure, which arises from the violent fracturing of the weak structure. The dominant frequency−amplitudes for group $S_{50}W_{50}$ and those for groups $S_{15}W_{85}$ and $S_{30}W_{70}$ evolve in similar patterns under cyclic loading at all levels until failure. The difference is that, for group $S_{50}W_{50}$, the overall amplitude increases slightly during the whole loading process, and the signal volume in the middle- and high-frequency regions jumps; in contrast, for groups $S_{70}W_{30}$ and $S_{85}W_{15}$, the increase is more significant, and a large number of high amplitudes over 62 dB can be observed before failure, which is indicative of internal damage to the strong structure. For group $S_{85}W_{15}$, massive high-amplitude signal clusters are concentrated before failure, meaning that the strong structure is severely damaged at this moment. In addition, for group $S_{70}W_{30}$, the AE signals are mainly concentrated in the high-frequency region, and the signal volume in the middle- and low-frequency regions plunges. In particular, group $S_{85}W_{15}$ has a large number of signal clusters in the range of 270−370 kHz. Scholars[43,44] pointed out that shear damage often presents low-frequency waveforms, while tensile damage usually corresponds to high-frequency waveforms. Therefore, it can be inferred that as HR rises, the weak structure gradually transitions from shear damage to tensile damage. Shear damage mainly occurs under a large proportion of the weak structure, while tensile damage dominates under a small proportion of the weak structure.

4.3.3. AF−RA Distribution. To depict the damage mode in the damage process more precisely, the AF−RA distribution of AE waveforms during sample loading was introduced,[45] where AF refers to the average frequency, and RA refers to the ratio of rising time to amplitude.[46] Previous studies disclosed that the AE waveforms of tensile damage usually show short rising time and high frequency, while those of shear damage display long rising time and low frequency. Figure 12 exhibits the AF−RA data density distribution, and the black dashed line (AF = 66.67 RA) is the dividing line to distinguish tensile damage from shear damage (Figure 13a). From Figure 12, the AF−RA high-density areas for groups $S_{15}W_{85}$ and $S_{30}W_{70}$ are mainly located at the lower right of the dashed line (extending along the RA axis). When the HR rises, the high-density area gradually shifts to the upper right of the dashed line (developing along the AF axis). The AF−RA data were counted according to the method in Figure 13a, and the percentages of tensile and shear damage were obtained (Figure 13b). From Figure 13b, it can be seen that the percentage of tensile damage gradually grows with the increase in HR, while that of shear damage gradually declines. For group $S_{15}W_{85}$, tensile damage accounts for 24.65%, while for group $S_{85}W_{15}$, it accounts for 85.55%. Under a large HR value ($S_{85}W_{15}$), the particles inside the weak structure are highly compacted under the high stress; resultantly, the sample can no longer deform along the axial direction, but it can still deform along the radial direction (Figure 8), thus producing more tensile damage. Therefore, the variation in AF−RA values, combined with coal rock mechanics, elastic dynamics, and gas geology, can be used to research and develop efficient outburst early warning technologies. The strong−weak coupling structure outburst prevention technology contributes to monitoring and assessing the outburst hazard in the roadway in real-time.

4.4. Failure Morphological Characteristics. Figure 14 shows the failure morphologies of samples with different HRs. It can be seen that the weak structure of group $S_{15}W_{85}$ fractures along the two penetrating shear cracks, and each part can maintain a high degree of integrity after failure. As the HR

https://doi.org/10.1021/acsomega.3c08786
ACS Omega 2024, 9, 17076−17088

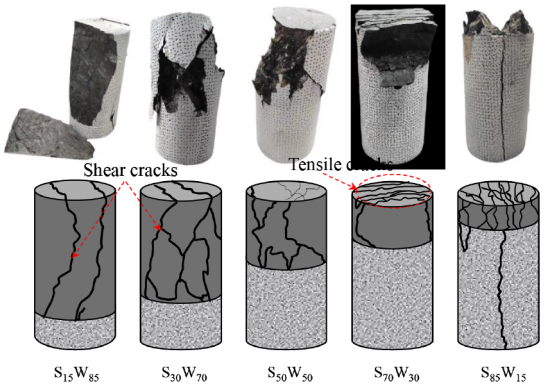

Figure 14. Failure morphologies of samples with different HRs.

rises, the cracks in the weak structure gradually increase, and the degree of integrity gradually declines after failure. It is noted that there are multiple tensile cracks at the end of the weak structure of group $S_{70}W_{30}$, and the weak structure of group $S_{85}W_{15}$ has the largest degree of fragmentation, and its strong structure is penetrated by a tensile crack. This is because, as the HR rises, the weak structure expands laterally to a higher extent, resulting in tensile damage to the strong structure. The above finding verifies the conclusion drawn in the above analysis on AE frequency−amplitude distribution; namely, the weak structure gradually transitions from shear damage to tensile damage with the increase in HR.

4.5. Failure Mechanism of Strong−Weak Coupling Samples with Different HRs. Based on the above phenomena, the failure mechanism of strong−weak coupling samples with different HRs was discussed in this section. Under axial pressure σ_1, the strong and weak structures expand laterally during loading. As the HR rises, the failure strength of the strong−weak coupling samples increases gradually. Due to the difference in the Poisson effect of the strong and weak structures, the lateral expansion capacity of the weak structure is significantly larger than that of the strong structure, inducing a friction effect at the interface. Meanwhile, the enhancement of ductility of the weak structure promotes the friction effect. Therefore, the weak structure exerts a friction force σ_{FW} from the center of the interface to the vicinity of the strong structure, while the strong structure applies a friction force σ_{FS} to the weak structure that prevents its lateral expansion. Ultimately, the strong structure gradually transitions from a unidirectional stress state to a triaxial tensile−compressive stress state[47] (Figure 15a). Study revealed that the tensile strength of rock mass materials is about 1/10 of their compressive strength.[48] Hence, a strong structure is more likely to fail under tension. The strong structure will stretch when the tensile stress reaches the critical value of tensile damage, whereas it will undergo only a gradual transition from tensile shear damage to tensile damage if the critical value is not reached. The failure mechanism of strong−weak coupling samples with different HRs is illustrated in Figure 15b.

5. CONCLUSIONS

This study aims to reveal the deformation and failure characteristics of strong−weak coupling samples with different HRs under cyclic loading and unloading using DIC and AE technologies in the hope of providing guidance on how to prevent strong−weak coupling outburst on site. The following conclusions are drawn:

(1) As the HR rises, the failure strength of the strong−weak coupling samples gradually increases under cyclic loading and unloading, suggesting that raising the grouting range can effectively improve the bearing capacity of the roadway. The residual strain of the strong−weak structure experiences three stages, i.e., the decelerated deformation, the constant-velocity deformation, and the accelerated deformation. Deformation mainly occurs in the weak structure, and the sample damage tends to start first from the strong−weak interface with the increase in the HR. When the HR increases to 85:15, the strong structure undergoes tensile damage.

(2) The AE signal shows strong regional distribution characteristics and the Felicity effect, with the damage concentrated near 70% of each stage in the cyclic loading process. With the increase of HR, the weak structure

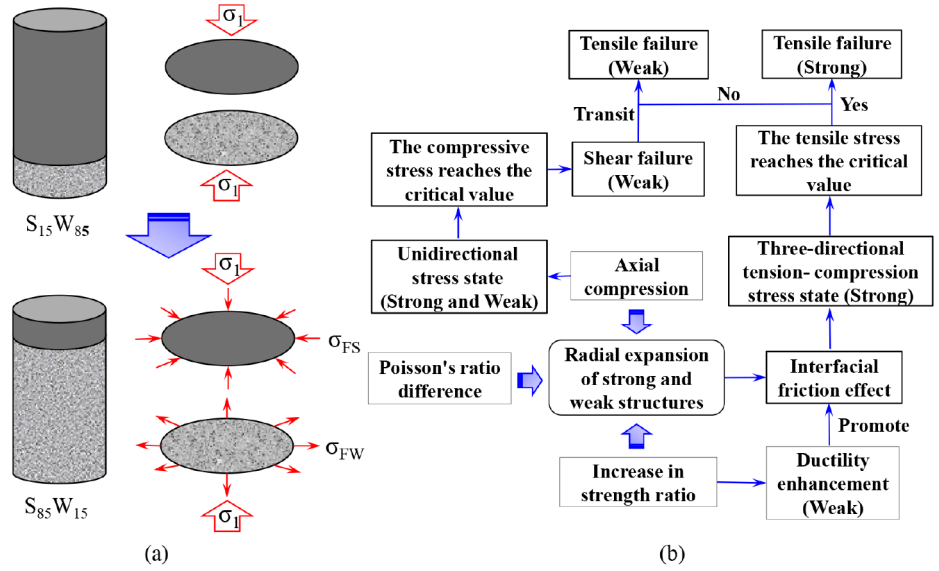

Figure 15. Stress state and failure mechanism of samples with different HRs, where (a), (b) denote the force state and failure mechanism of the samples, respectively.

https://doi.org/10.1021/acsomega.3c08786
ACS Omega 2024, 9, 17076−17088

transitions from brittle damage to ductile damage, and the percentage of tensile damage gradually increases. Due to the difference in Poisson effects of the strong and weak structures, under a larger HR ($S_{85}W_{15}$), the strong and weak structures generate the breaking friction effect at the interface, which leads to tensile damage of the strong structure.

(3) With respect to the field application of strong−weak coupling outburst prevention, the weak structure corresponds to the broken coal body, while the strong structure is actually the coal and cement slurry combination, which differs from this study. Therefore, it is necessary to develop an experimental method that is more in line with the field conditions in the future.

AUTHOR INFORMATION

Corresponding Author

Cheng Zhai − *School of Safety Engineering and Research Center for Coal Mine Gas Control, China University of Mining and Technology, Xuzhou, Jiangsu 221116, China; Key Laboratory of Coal Methane and Fire Control, Ministry of Education, China University of Mining and Technology, Xuzhou, Jiangsu 221116, China;* orcid.org/0000-0001-9256-1494; Phone: +8613585391210; Email: greatzc@cumt.edu.cn

Authors

Aikun Chen − *School of Safety Engineering and Research Center for Coal Mine Gas Control, China University of Mining and Technology, Xuzhou, Jiangsu 221116, China; Key Laboratory of Coal Methane and Fire Control, Ministry of Education, China University of Mining and Technology, Xuzhou, Jiangsu 221116, China*

Xu Yu − *School of Safety Engineering and Research Center for Coal Mine Gas Control, China University of Mining and Technology, Xuzhou, Jiangsu 221116, China; Key Laboratory of Coal Methane and Fire Control, Ministry of Education, China University of Mining and Technology, Xuzhou, Jiangsu 221116, China;* orcid.org/0000-0002-5354-6723

Yangfeng Zheng − *School of Safety Engineering and Research Center for Coal Mine Gas Control, China University of Mining and Technology, Xuzhou, Jiangsu 221116, China; Key Laboratory of Coal Methane and Fire Control, Ministry of Education, China University of Mining and Technology, Xuzhou, Jiangsu 221116, China*

Yuzhou Cong − *School of Safety Engineering and Research Center for Coal Mine Gas Control, China University of Mining and Technology, Xuzhou, Jiangsu 221116, China; Key Laboratory of Coal Methane and Fire Control, Ministry of Education, China University of Mining and Technology, Xuzhou, Jiangsu 221116, China*

Jianguo Wu − *Kailuan (Group) Limited Liability Corporation, Tangshan, Hebei 130200, China*

Complete contact information is available at: https://pubs.acs.org/10.1021/acsomega.3c08786

Notes

The authors declare no competing financial interest.

ACKNOWLEDGMENTS

This research was financially supported by National Key R&D Program of China (2020YFA0711800), The National Science Fund for Distinguished Young Scholars (51925404), Postgraduate Pesearch & Practice Innovation Program of Jiangsu Province (KYCX22_2662), and Assistance Program for Future Outstanding Talents of China University of Mining and Technology (2022WLJCRCZL17).

REFERENCES

(1) National Bureau of Statistics of the People's Republic of China. *Development of the people's republic of China in 2021*; Statistical Bulletin of National Economic and Social Development, 2022.

(2) Zhang, X.; Tang, J. P.; Pan, Y. S.; Yu, H. H. Experimental study on intensity and energy evolution of deep coal and gas outburst. *Fuel* **2022**, *324*, 124484.

(3) Li, L. J.; Liu, D. M.; Cai, Y. D.; Wang, Y. J.; Jia, Q. F. Coal structure and its implications for coalbed methane exploitation: A Review. *Energy Fuel* **2021**, *35* (1), 86−110.

(4) Tu, Q. Y.; Xue, S.; Cheng, Y. P.; Zhang, W.; Shi, G. F.; Zhang, G. Experimental study on the guiding effect of tectonic coal for coal and gas outburst. *Fuel* **2022**, *309*, 122087.

(5) An, F. H.; Yuan, Y.; Chen, X. J.; Li, Z. Q.; Li, L. Y. Expansion energy of coal gas for the initiation of coal and gas outbursts. *Fuel* **2019**, *235*, 551−557.

(6) Lei, Y.; Cheng, Y. P.; Ren, T.; Tu, Q. Y.; Li, Y. X.; Shu, L. Y. Experimental investigation on the mechanism of coal and gas outburst: Novel insights on the formation and development of coal spallation. *Rock Mech. Rock Eng.* **2021**, *54* (11), 5807−5825.

(7) Huang, Y.; Yang, W.; Li, Y.; Guo, W. Spatial Distribution Characteristics of plastic failure and grouting diffusion within deep roadway surrounding rock under three-dimensional unequal ground stress and its application. *Minerals* **2022**, *12* (3), 296.

(8) Zhiqiang, Y.; Zhiyu, C.; Jucai, C.; Zuxiang, H.; Haifeng, M.; Ruimin, F. Crack initiation characteristics of gas-containing coal under gas pressures. *Geofluids* **2019**, *2019*, 1−12.

(9) Guanhua, N.; Hui, W.; Baisheng, N.; Yan, W.; Haoran, D.; Shouqing, L.; Gang, W.; et al.et al. Research of wetting selectivity and wetting effect of imidazole ionic liquids on coal. *Fuel* **2021**, *286*, 119331.

(10) Wang, E. Y.; Zhang, G. R.; Zhang, C. L.; Li, Z. H. Research progress and prospect on theory and technology for coal and gas outburst control and protection in China. *J. China Coal Soc.* **2022**, *47* (1), 297−322.

(11) Qin, Y. J.; Jin, K.; Tian, F. C.; Su, W. W.; Ren, S. K. Effects of ultrathin igneous sill intrusion on the petrology, pore structure and ad/desorption properties of high volatile bituminous coal: Implications for the coal and gas outburst prevention. *Fuel* **2022**, *316*, 123340.

(12) Pan, W.; Changwen, H.; Xuelong, L.; Shoujian, P.; Yanan, L. Numerical simulation of boreholes for gas extraction and effective range of gas extraction in soft coal seams. *Energy Sci. Eng.* **2019**, *7* (5), 1632−1648.

(13) Dong, K.; Ni, G. H.; Nie, B. S.; Xu, Y.; Wang, G.; Sun, L.; Liu, Y.; et al.et al. Effect of polyvinyl alcohol/aluminum microcapsule expansion agent on porosity and strength of cement-based drilling sealing material. *Energy* **2021**, *224*, 224.

(14) Lyu, S. F.; Wang, S. W.; Li, J. Y.; Chen, X.; Chen, L.; Dong, Q.; Zhang, X.; Huang, P.; et al.et al. Massive Hydraulic Fracturing to control gas outbursts in soft coal seams. *Rock Mech. Rock Eng.* **2022**, *55* (3), 1759−1776.

(15) Zhang, H.; Cheng, Y. P.; Deng, C. B.; Shu, L.; Pan, Z.; Yuan, L.; Wang, L.; Liu, Q.; et al.et al. A novel in-seam borehole discontinuous hydraulic flushing technology in the driving face of soft coal seams: Enhanced gas extraction mechanism and field application. *Rock Mech. Rock Eng.* **2022**, *55* (2), 885−907.

(16) Zhang, H.; Cheng, Y. P.; Yuan, L.; Wang, L.; Pan, Z. J. Hydraulic flushing in soft coal sublayer: Gas extraction enhancement mechanism and field application. *Energy Sci. Eng.* **2019**, *7* (5), 1970−1993.

https://doi.org/10.1021/acsomega.3c08786
ACS Omega 2024, 9, 17076−17088

(17) Shen, R. X.; Zhang, X.; Wang, E. Y.; Li, H. R.; Han, X.; Hou, Z. H. Application of acoustic emission technique to the evaluation of coal seam hydraulic flushing effect. *Energies* **2019**, *12* (9), 1705.
(18) Wang, W.; Wang, G.; Zhao, W.; Wang, L.; Feng, Z.; Cui, R.; Du, F.; et al.et al. Numerical assessment of the pressure relief effect of the hydraulic punching cavitation technique in a soft coal seam. *Geomech. Geophys. Geo. Energy Geo. Resour.* **2022**, *8* (1), 1−18.
(19) Zheng, Z.; Li, S. C.; Liu, R. T. Analysis on structural characteristics of grout and rock distribution in complex geological mixtures after grouting reinforcement and its mechanical strength. *Rock Mech. Rock Eng.* **2021**, *54* (8), 3757−3782.
(20) Wang, H.; Jiang, C.; Zheng, P. Q.; Li, N.; Zhan, Y. B. Deformation and failure mechanism of surrounding rocks in crossed-roadway and its support strategy. *Eng. Failure Anal.* **2020**, *116*, 104743.
(21) Zheng, Y. F.; Zhai, C.; Zhang, J. G.; Yu, X.; Xu, J.; Sun, Y.; Cong, Y.; Tang, W. Deformation and fracture behavior of strong−weak coupling structure and its application in coal roadway instability prevention. *Fatigue. Fract. Eng. Mater. Struct.* **2022**, *45* (1), 203−221.
(22) Sha, F.; Lin, C. J.; Li, Z. F.; Liu, R. T. Reinforcement simulation of water-rich and broken rock with portland cement-based Grout. *Constr. Build. Mater.* **2019**, *221*, 292−300.
(23) Chen, Y. L.; Zuo, J. P.; Liu, D. J.; Wang, Z. B. Deformation failure characteristics of coal−rock combined body under uniaxial compression: Experimental and numerical investigations. *B Eng. Geol. Environ.* **2019**, *78* (5), 3449−3464.
(24) Xie, Z. Z.; Zhang, N.; Meng, F. F.; Han, C. L.; An, Y. P.; Zhu, R. J. Deformation field evolution and failure mechanisms of coal−rock combination based on the digital speckle correlation method. *Energies* **2019**, *12* (13), 2511.
(25) Gong, F.; Ye, H.; Luo, Y. The effect of high loading rate on the behaviour and mechanical properties of coal-rock combined body. *Shock Vib.* **2018**, *2018*, 1−9.
(26) Wang, T. N.; Zhai, Y.; Gao, H.; Li, Y. B.; Zhao, R. F. A novel binary effective medium model to describe the prepeak stress-strain relationship of combined bodies of rock-like material and rock. *Int. J. Min. Sci. Technol.* **2023**, *33* (5), 601−616.
(27) Hao, Z.; Jian, K. L.; Peng, S. J.; Xu, J. Numerical investigation of coal and gas outbursts under different in situ stresses and gas pressures and the physical characteristics of coal. *ACS Omega* **2021**, *6* (20), 13260−13274.
(28) Gao, D. Y.; Sang, S. X.; Liu, S. Q.; Wu, J.; Geng, J.; Tao, W.; Sun, T. Experimental study on the deformation behaviour, energy evolution law and failure mechanism of tectonic coal subjected to cyclic loads. *Int. J. Min. Sci. Technol.* **2022**, *32* (6), 1301−1313.
(29) Yu, G. F.; Cheng, G. W.; Li, L. C.; Tang, C. A.; Ren, B.; Han, Y. C. Preliminary study on high-energy and low-energy microfracture event evolution characteristics in the development process of rock failure. *Geofluids* **2020**, *2020*, 1−17.
(30) Gao, M. S.; Zhao, Y. C.; Wen, Y. Y.; Cheng, Z. C.; Quan, X. C. Stress and energy criterion of the roadway destruction subjected to disturbance type rock burst and its practice. *J. China Coal Soc.* **2016**, *41* (4), 808−814.
(31) Gao, M. S.; He, Y. L.; Lu, C. P.; Shao, X.; Yang, Z. Coordination mechanism of internal strong active support, soft structure pressure relief and anti-punching of roadway. *J. China Coal Soc.* **2020**, *45* (8), 2749−2759.
(32) Zheng, Y. F.; Zhai, C.; Xin, H. H.; Tang, W.; Sun, Y.; Xu, J. Z. Theories and methods of coal and gas outburst prevention by strong-weak coupling energy control in coal roadway driving face. *J. Min. Saf. Eng.* **2021**, *38* (6), 1269−1280.
(33) Niu, Y.; Zhou, X. P.; Zhou, L. S. Fracture damage prediction in fissured red sandstone under uniaxial compression: Acoustic emission *b*-value analysis. *Fatigue. Fract. Eng. Mater. Struct.* **2020**, *43*, 175−190.
(34) Cong, Y. Z.; Zhai, C.; Sun, Y.; Xu, J. Z.; Tang, W.; Zheng, Y. F. Visualized study on the mechanism of temperature effect on coal during liquid nitrogen cold shock. *Appl. Therm. Eng.* **2021**, *194*, 116988.
(35) Xiu, Z. G.; Wang, S. H.; Ji, Y. C.; Wang, F. L.; Ren, F. Y.; Nguyen, V. T. Loading rate effect on the uniaxial compressive strength (UCS) behavior of cemented paste backfill (CPB). *Constr. Build. Mater.* **2021**, *271*, 121526.
(36) He, J. H.; Li, Y.; Deng, H. C.; Tang, J. M.; Wang, Y. Y. Quantitative evaluation and influencing factors analysis of the brittleness of deep shale reservoir based on multiply rock mechanics experiments. *J. Nat. Gas Geosci.* **2022**, *7* (5), 295−307.
(37) Liu, X. Y.; Yu, J.; Zhu, Y. L.; Yao, W.; Lai, Y. M. Creep damage evolution of marble from acoustic emission and the damage threshold. *Front. Earth Sci.* **2020**, *8*, 58.
(38) Yang, D. J.; Hu, J. H.; Ma, S. W.; Zeng, P. P. Analysis of dynamic fracture of franite after uniaxial recompression predamaged by high confining pressure cyclic loading based on acoustic emission. *Eng. Fract. Mech.* **2022**, *266*, 108414.
(39) Chai, M. Y.; Hou, X. L.; Zhang, Z. X.; Duan, Q. Identification and prediction of fatigue crack growth under different stress ratios using acoustic emission data. *Int. J. Fatigue* **2022**, *160*, 106860.
(40) Qu, H.; Wu, X. G.; Huang, P. P.; Tang, S. M.; Wang, R.; Hu, Y. S. Acoustic emission and failure characteristics of shales with different brittleness under AEJ impingement. *Rock Mech. Rock Eng.* **2022**, *55* (4), 1871−1886.
(41) Wang, C. Y.; Chang, X. K.; Liu, Y. L.; Chen, S. J. Mechanistic characteristics of double dominant frequencies of acoustic emission signals in the entire fracture process of fine sandstone. *Energies* **2019**, *12* (20), 3959.
(42) Duan, M. K.; Jiang, C. B.; Gan, Q.; Li, M. H.; Peng, K.; Zhang, W. Experimental investigation on the permeability, acoustic emission and energy dissipation of coal under tiered cyclic unloading. *J. Nat. Gas. Sci. Eng.* **2020**, *73*, 103054.
(43) Miao, S. T.; Pan, P. Z.; Zhao, X. G.; Shao, C. Y.; Yu, P. Y. Experimental study on damage and fracture characteristics of beishan granite subjected to high-temperature treatment with DIC and AE techniques. *Rock Mech. Rock Eng.* **2021**, *54* (2), 721−743.
(44) Aggelis, D. G.; Mpalaskas, A. C.; Matikas, T. E. Acoustic signature of different fracture modes in marble and cementitious materials under flexural load. *Mech. Res. Commun.* **2013**, *47*, 39−43.
(45) Du, K.; Li, X.; Tao, M.; Wang, S. Experimental study on acoustic emission (AE) characteristics and crack classification during rock fracture in several basic lab tests. *Int. J. Rock Mech. Min.* **2020**, *133*, 104411.
(46) Zhang, X.; Li, Z.; Wang, X.; Wang, H.; Li, B.; Niu, Y. Thermal effect on the fracture behavior of granite using acoustic emission and digital image correlation: An experimental investigation. *Theor. Appl. Fract. Mech.* **2022**, *121*, 103540.
(47) Chen, S. J.; Yin, D. W.; Zhang, B. L.; Ma, H. F.; Liu, X. Q. Mechanical characteristics and progressive failure mechanism of roof-coal pillar structure. *Chin. J. Rock Mech. Eng.* **2017**, *36* (7), 1588−1598.
(48) Hamidi, F.; Aslani, F.; Valizadeh, A. Compressive and tensile strength fracture models for heavyweight geopolymer concrete. *Eng. Fract. Mech.* **2020**, *231*, 107023.

https://doi.org/10.1021/acsomega.3c08786
ACS Omega 2024, 9, 17076−17088